Using the inertia of spacecraft during landing to penetrate regoliths of the Solar System

Using the inertia of spacecraft during landing to penetrate regoliths of the Solar System

M. D. Paton**

Finnish Meteorological Institute, PO Box 503, FIN-00101 Helsinki, Finland

S. F. Green, A. J. Ball

Department of Physical Sciences, The Open University, Milton Keynes, MK7 6AA, UK

J. C. Zarnecki

International Space Science Institute, 3012 Bern, Switzerland

A. -M. Harri

Finnish Meteorological Institute, PO Box 503, FIN-00101 Helsinki, Finland

Abstract

The high inertia, i.e. high mass and low speed, of a landing spacecraft has the potential to drive a penetrometer into the subsurface without the need for a dedicated deployment mechanism, e.g., during Huygens landing on Titan. Such a method could complement focused subsurface exploration missions, particularly in the low gravity environments of comets and asteroids, as it is conducive to conducting surveys and to the deployment of sensor networks. We make full-scale laboratory simulations of a landing spacecraft with a penetrometer attached to its base plate. The tip design is based on that used in terrestrial Cone Penetration Testing (CPT) with a large enough shaft diameter to house instruments for analysing pristine subsurface material. Penetrometer measurements are made in a variety of regolith analogue materials and target compaction states. For comparison a copy of the ACC-E penetrometer used on the Huygens mission is used. A test rig at the Open

*Corresponding author

**Phone: +358 50 4302984

Email address: mark.paton@fmi.fi (M. D. Paton)

University is used and is operated over a range of speeds from 0.9 to 3 m s^{-1} and under two gravitational accelerations.

The penetrometer was found to be sensitive to the target's compaction state with a high degree of repeatability. The penetrometer measurements also produced unique pressure profile shapes for each material. Measurements in limestone powder produced an exponential increase in pressure with depth possibly due to increasing compaction with depth. Measurements in sand produced an almost linear increase in pressure with depth. Iron powder produced significantly higher pressures than sand presumably due to the rough surface of the grains increasing the grain-grain friction. Impacts into foamglas produced with both ACC-E and the large penetrometer produced an initial increase in pressure followed by a leveling off as expected in a consolidated material. Measurements in sand suggest that the pressure on the tip is not significantly dependent on speed over the range tested, which suggests bearing strength equations could be applied to impact penetrometry in sand-like regoliths.

In terms of performance we find the inertia of a landing spacecraft, with a mass of 100 kg, is adequate to penetrate regoliths expected on the surface of Solar System bodies. Limestone powder, an analogue for a dusty surface, offered very little resistance allowing full penetration of the target container. Both iron powder, representing a stronger coarse grained regolith, and foamglas, representing a consolidated comet crust, could be penetrated to similar depths of around two to three tip diameters, probably more if impacting with a slightly higher speed.

Keywords: penetrometer, spacecraft, landing, asteroid, comet, subsurface

---

1. Introduction

A landing spacecraft, at the moment of touchdown, will decelerate in response to the mechanical properties of the planetary surface and the structure of the spacecraft. By measuring the dynamic forces on a protrusion from the spacecraft, that is rigid compared to the surface, penetrometry measurements can be made that are useful for investigating the macro and micro scale properties of the regolith. Impact penetrometry has been used successfully on several space missions (Ball et al., 2010) including the Surveyor (Jones, 1971) and Huygens (Zarnecki et al., 2005) missions. A future application could be, for example, an end of mission landing on a near-Earth asteroid

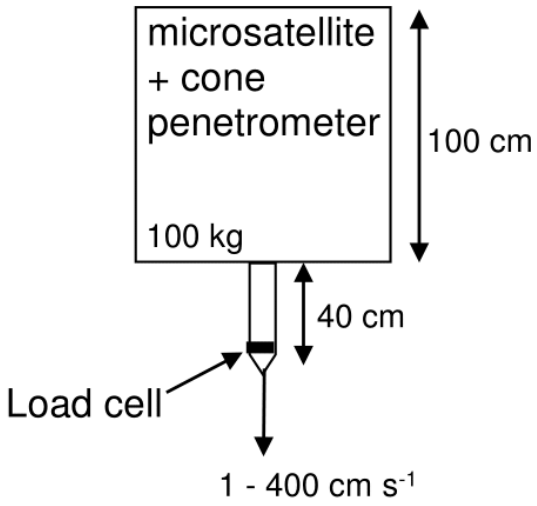

Figure 1: Large impact penetrometer for spacecraft considered in this study. The illustration shows a spacecraft not designed for landing fitted with a large penetrator that acts as an impact penetrometer and provides subsurface access for instruments to characterise the subsurface. The large penetrator could assist landing of the spacecraft keeping the g-loading low.

like the NEAR landing on Eros, or perhaps the deployment of a penetrometer microstation that could be useful for asteroid surveys and setting up of sensor networks. A penetrometer fitted to the base of a spacecraft as shown in figure 1, if large enough, could also double as a braking device to allow higher landing speeds than normal, similar in principle to the MetNet lander for a ballistic landing on Mars (Harri et al., 2014). This approach could be used on an asteroid, for example, if the thrust of a spacecraft engine cannot counter gravity or the spacecraft is low on fuel. After the landing thermal investigations of the sub-surface using sensors and instruments housed in a penetrometer could be made to further characterise the subsurface and monitor its properties over time (Paton et al., 2010, 2012b). If a controlled landing is possible in a low gravity environment, by using the spacecraft thrusters, a detachable penetrometer fitted with a battery and antenna could in principle be left in the regolith while the spacecraft returns to survey the asteroid from orbit.

The scope of this paper is to investigate the response of the penetrometer to different regolith materials, to determine the reachable depths of material

of different strengths and the potential g-loads on the spacecraft. Within that context there will be some limited analysis of the penetrometry measurements to identify whether existing interpretation techniques can be used. The paper is structured as follows. In section 2 we compare various impact penetrometry measurements made remotely by spacecraft. We consider previous designs and propose an approach for utilising an impact penetrometer in a low gravity environment. A test rig is described in section 3 that is used to conduct experiments simulating landings on asteroids and Titan of a spacecraft fitted with an impact penetrometer. The two penetrometers used in the experiments are also described in section 3 together with the target and experimental approach. In section 4 a penetration equation is described that is used to analyse the results. Section 5 presents results from the large experimental penetrometer (X-PEN) and a copy of the smaller Huygens penetrometer (ACC-E). The penetrometer measurements are plotted with penetration depth data obtained using a shaft encoder attached to the test rig. The plots are described in terms of their notable and prominent features. In section 6 the penetrometer measurements are assessed in terms of mechanical processes and compaction during penetration. The g-level loadings on the simulated spacecraft are derived from the penetrometer measurements. Extrapolation of these results to higher speeds is discussed. Applicability of the technique is investigated with simple penetration modelling using equation 1 from section 2 and discussed briefly in terms of three different classes of Solar System bodies, i.e. asteroids and comets, large airless worlds and worlds with atmospheres.

2. Subsurface exploration possibilities using penetrometers and penetrators

Penetrometry measurement techniques are often tailored to the mission to optimise the scientific return and may require additional information from other instruments when investigating underexplored terrain due to the point nature of the measurement, e.g., (Zarnecki et al., 2005). Penetrometry utilising parts of the spacecraft structure, such as landing pads, is limited to the top few centimetres of the surface and is useful for determining bearing capacity and for insights into weathering and volatile exchange processes. Such investigations into the top centimetres of a regolith, shown in figure 2, were performed on the Moon by the Surveyor landing legs (Jones, 1971) and on Titan by the Huygens probe with a penetrometer mounted on its base

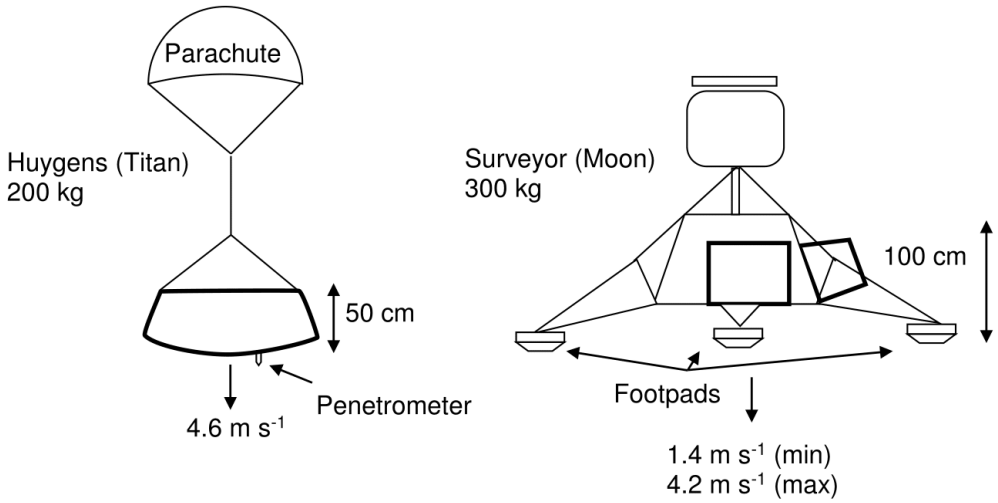

Figure 2: Examples of spacecraft that have conducted penetrometry investigations during landing.

(Lorenz et al., 1994). A penetrometer, deployed from the spacecraft, such as the MUPUS thermal probe (Spohn et al., 2007), can allow deeper access perhaps reaching layers that are insulated from surface processes and provide information on long-term processes.

Penetrators look similar to a detached penetrometer in appearance, but are self-contained spacecraft, whose depth of penetration is not limited by a deployment mechanism but other factors such as communication signal strength reduction due to burial may require that the penetrator remains near the surface. Planetary penetrators such as the Mars 96 (Surkov & Kremnev, 1998) and Deep Space 2 (Smrekar et al., 1999), shown in figure 3, were both lost after launch under different circumstances. However, extensive testing suggests useful information can be obtained from these devices. Penetrators can house an array of sophisticated instruments within their body. For example, the Mars 96 penetrators included a gamma-ray spectrometer, x-ray spectrometer, neutron spectrometer, accelerometer, the-

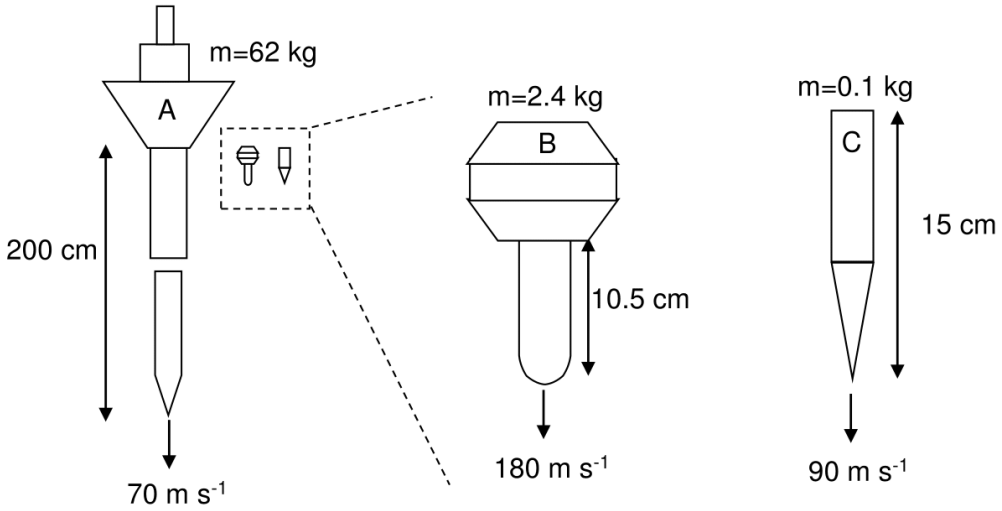

Figure 3: Examples of high speed planetary penetrators. (a) Mars 96 penetrator (b) Deep Space 2 penetrator and (c) Philae anchor. For a more comprehensive selection of penetrators see figure 1 in Lorenz (2011).

mocouples, seismometer and magnetometer, TV camera and meteorological sensor to comprehensively characterise the Martian environment. Various impact penetrometry techniques are listed in table 1 comparing their performance in terms of momentum, dimensions, tip depth and g-loading. Note the low speed heavy landers like Surveyor and Huygens have comparable momentum to the high speed, low mass penetrators but do not penetrate as far. This is because they have a much larger diameter and hence drag area.

A large penetrometer driven into the surface using the inertia of a landing spacecraft as proposed here is a technique that encompasses the merits of both penetrometers and penetrators. The slow speed during landing would also allow the inclusion of instruments inside or on the penetrometer shaft without the need for added shock absorption measures typically required for high speed penetrators. The penetrometer would likely be able to determine microstructural information such as grain size and mass (Paton et al., 2012a) which may be difficult at high speeds due to sampling rate limitations. Such a spacecraft impact penetrometer deployment approach does not require a reaction mass or stable host spacecraft for conducting penetrometry and it could be used in low gravity environments, as found on asteroids.

Table 1: Selected list of spacecraft impact penetrometry missions and their basic configurations and impact information. Further information on penetrometry in the Solar System can be found in Kargl et al. (2009); Kömle et al. (2001b). Ball et al. (2010) contains an overview of planetary landers including penetrators.

Name	Impact velocity ($m\ s^{-1}$)	Mass (kg)	Momentum ($kg\ m^{-1}$)	Diameter (cm)	Length (cm)	Depth (cm)	Max. g (g)
Mars 96	80	45	3600	12	150	600	1k
DS2	190	0.67	127	4	10.5	60	60k
Lunar-A	285	13.5	3847	16	80	300	15k
ACC-E (Huygens)	4.6	200	920	1.6	8	5	0.02
Anchor (Philae)	90	0.09	8.1	1.5	9	200	0.4k
Huygens	4.6	200	920	120	8	12	18
Surveyor	2-4	300	900	30	13	2-10	20-40

An additional application, if the attached penetrometer has a large cross-sectional area, is that it could make an effective brake, with low g-loadings on the payload, enabling an orbiter-type spacecraft to possibly perform unpowered free-fall landings on an asteroid. It could also assist landings on larger worlds such as Titan where an unpowered landing speed may be higher. Instruments such as thermal sensors and cameras could be mounted inside or on the penetrometer surface to make post-penetration measurements of the surrounding subsurface material similar to the MetNet concept (Harri et al., 2014).

A problem encountered when using penetrometers and penetrators is that they disturb the target material creating zones of disturbance around the penetrometer shaft and in front of the tip. Also, the mismatch between the target and penetrator's thermal properties and the shadow cast by the spacecraft make thermal measurements complicated.

A large penetrating device fixed to the base of a landing spacecraft could also complicate landing gear operations. Spacecraft often have a control system to prevent excessive movements after the initial touchdown. The Philae landing has shown this to be difficult, in the low gravity environment of a comet, bouncing three times before finally coming to rest (Hand, 2014). Also the deployment of the penetrator or penetrometer, in all likelihood, cannot be repeated as the penetrometer will probably become stuck in the regolith after penetration. Another potential complication is the large range

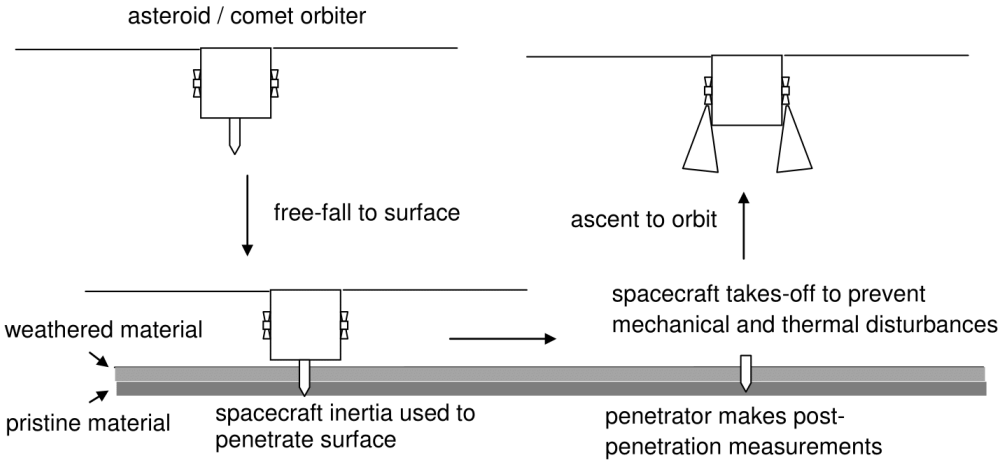

Figure 4: Possible emplacement of a large penetrator using the inertia of a spacecraft. The spacecraft detaches from the penetrator or penetrometer and ascends to orbit to prevent thermal and mechanical disturbances to the surrounding regolith. Also this approach would also prevent withdrawal of the penetrator due to a rebound caused by the elastic properties of the spacecraft structure.

of uncertainties of unexplored surface properties which will add risk to the operation.

A possible way to mitigate the thermal disturbances of the target is to use a detachable penetrometer allowing the spacecraft to ascend immediately after deployment. In a low gravitational environment a penetrometer could be left in the regolith with its own power and communication system as shown in figure 4. In addition to scientific enquiries this type of deployment would be useful for, e.g., a seismic network or securing a beacon for precision tracking of the asteroid. This approach could also help minimise the risk when landing on uncharacterised surfaces which may, for instance, include buried rocks. An impact with a rock buried in the regolith could potentially push the penetrometer into the spacecraft body and destroy it. To mitigate this risk a detatchable penetrometer could be designed to break off, under excessive stresses, enabling the main spacecraft to escape. This strategy may even preserve the penetrometer allowing it to perform some limited surface measurements.

Drills and hammer driven low velocity penetrators are some other promising techniques for subsurface exploration. Drilling has been used on a variety of missions to expose unweathered rock and collect samples, for example the Mars rover curiosity has a drill used for drilling into rock (Grotzinger et al., 2012). Hammer driven penetrators can be used to 'drill' into the surface. A promising technique for obtaining structural and stratigraphic information while drilling is using Seismic While Drilling (SWD) method (Coste et al., 2010). The Philae lander has used a hammer driven penetrator, with some success, to insert thermal sensors into the soft upper layer of a comet (Gibney, 2014; Seweryn et al., 2014).

3. Experimental method

3.1. Test rig

Ideally a spacecraft impact penetrometer needs to be tested in a gravitational environment similar to that on the target body, especially if the impact occurs in microgravity, in order to correctly simulate the impact mechanics in low gravity. In low gravity the impact mechanics for a granular material may be very different to the impact mechanics under Earth gravity as the shearing strength will be greatly reduced because of the lower gravitational acceleration (Daniels, 2013). However it is often impractical to make such simulations and spacecraft landings are often simulated with targets under Earth's gravity.

For our impact tests we make use of a test rig based on a modified Atwood machine developed at the Open University. The rig has been used to perform investigations of landings on asteroids (Paton, 2005) and to interpret data from the Huygens' penetrometer on Titan (Zarnecki et al., 2005). The rig, shown in figure 5, uses balanced weights linked in a loop to simulate full-scale landings of spacecraft on Solar System bodies in the laboratory. There are two sets of chain loops running in parallel that enables a simulated spacecraft base plate and the weights to be mounted on a cross-beam between the chains at the front of the rig. At the back of the rig there is a similar arrangement with a cross-beam with weights mounted on it. The cross-beam has slider type trolleys each side running on vertically mounted rails with the chains connected to them. The balanced weights can be adjusted to simulate gravitational accelerations from zero up to that of Earth. The looped system ensures the equivalent inertia from both sets of weights is transferred to the target, simulating a rigid body with a total mass equal to the sum of the

two weights. The test rig can be accelerated up to impact speed by a set of accelerating weights that disengage from the system before the impact of the penetrometer.

A spacecraft mass, m, of about 100 kg was used for tests in a simulated microgravity environment of an asteroid or comet as this is the mass of a typical microsatellite. The effective spacecraft mass is the total of the moving parts of the rig. To simulate impacts on km-sized bodies, weights were placed on the front and rear bars so that each side was balanced (see figure 5). For simulations of impacts on Titan the total mass was smaller, to allow higher impact speeds, and the front mass was out of balance with the back to simulate gravity on Titan.

On the test rig resides a shaft encoder for measuring distance and speed. The shaft encoder is attached to one of the test rig shafts and produces a square-wave pulse each time the shaft rotates a certain amount. The shaft encoder can also be used to determine distance and speed with uncertainties of ± 5 mm and ± 4 cm s^{-1} respectively. Measurement errors with the shaft encoder are due to calibration uncertainties, ADC signal digitization, ADC sampling frequency and small mechanical oscillations in the test rig chain. Calibration uncertainties accumulate when summing the shaft encoder pulses to calculate distance. ADC digitization does not adversely affect shaft encoder output as it is binary, i.e. high voltage or low voltage.

3.2. Experimental impact penetrometer (X-PEN)

Pressure measurements in analogue regolith materials are made by an eXperimental impact PENetrometer (X-PEN) as shown in figure 6. A 10 kN Entran ELW series load cell is fitted behind the cone to measure pressure. The sensor is a semiconductor strain gauge whose resistance varies with load. It was originally designed (Paton, 2005) to make low speed impact penetrometry measurements and subsurface thermal measurements. The tip dimensions are the same as used in the Cone Penetration Test (CPT) which is standardised to ASTM standards. CPT is used for soil profiling in the civil engineering industry, identifying soil types, profiling sub-surface stratification and determine bearing capacity and consequently a large database of knowledge is available for possible utilisation in interpretation of X-PEN data. The length of the penetrometer was chosen from considerations of the possible thermal skin depths expected on a planetary surface and the desire to access pristine material. The shaft was polished to minimise the frictional forces from the target.

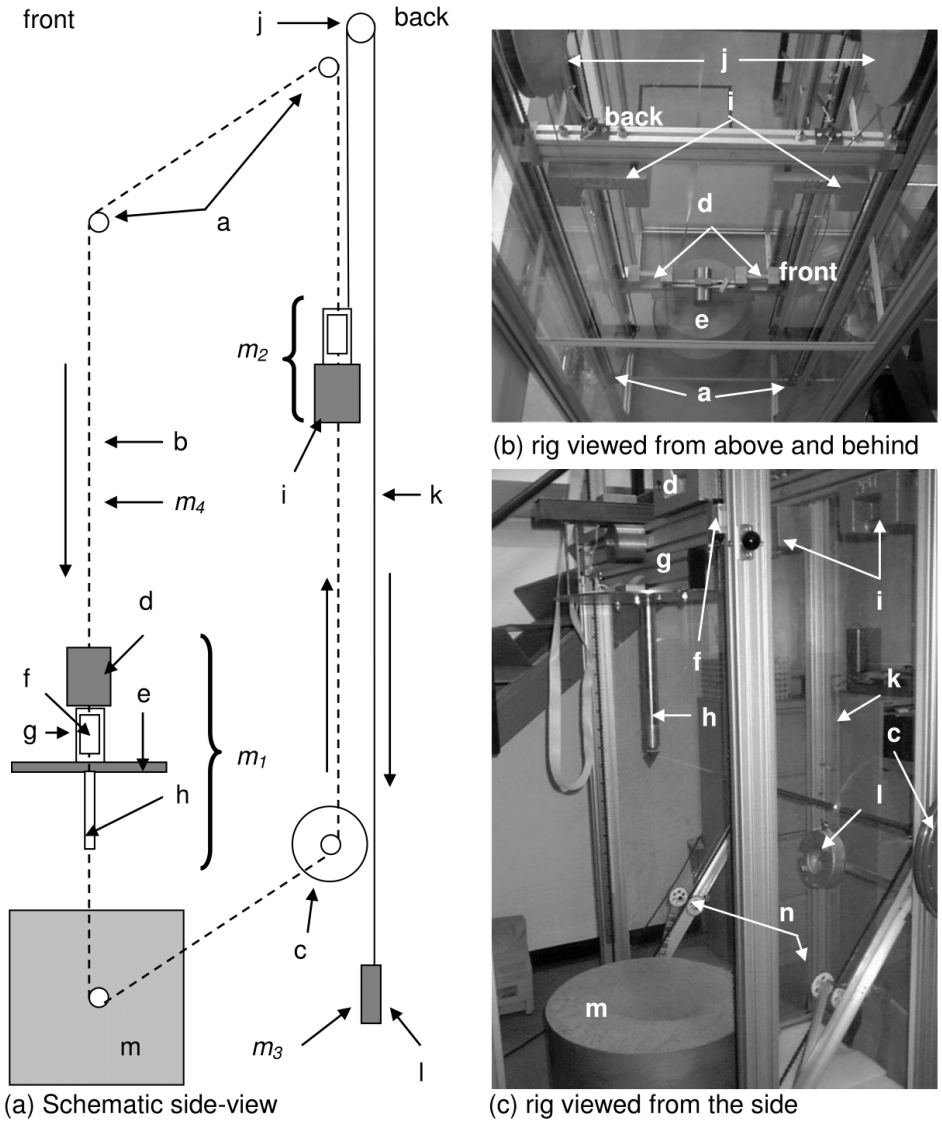

Figure 5: Laboratory simulation of a spacecraft landing using a test rig (Paton, 2005). The schematic on the left shows the principle of operation using a loop to simulate the inertia of a rigid body and balancing weights to balance out Earth's gravity. On the right is the rig in the laboratory with a large penetrometer attached to the simulated spacecraft base. (a) are the cogs, (b) chain, (c) operators winding handle, (d) front weights (e) base plate, (f) trolley, (g) front cross-beam structure, (h) penetrometer, (i) backweights (j) accelerating mass roller (k) accelerating mass cable (l) accelerating weight (m) NEO analogue material and (n) chain devices. The front mass, m_1, back mass, m_2, accelerating mass, m_3, and chain mass

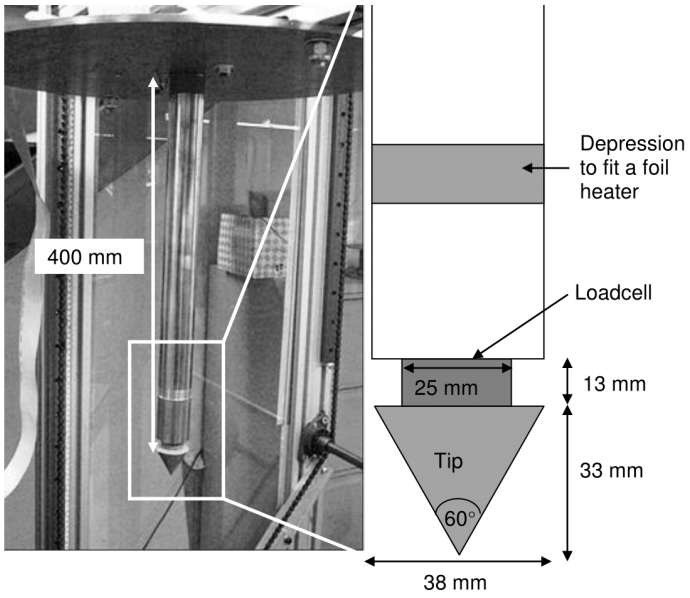

Figure 6: Experimental penetrometer attached to the test rig base plate. Components of the test rig can be seen in the background: the chain passing over a cog (lower right); the front beam (top). The experimental penetrometer is attached to the underside of the base plate. The depression in the shaft of the penetrometer was intended to contain a film heater for making thermal measurements. Thermal measurements using a thermal probe based on this design can be found in Paton et al. (2012b).

In CPT the penetrometer is inserted slowly at a constant rate of about 2 cm s^{-1} to avoid dynamic effects such as the generation of excessive pore pressure (Rogers, 2006). With our deployment technique, there may be dynamic effects somewhat similar to experienced in the Standard Penetration Test (SPT). The SPT conducts pentrometry by counting the number of hammer blows to push the penetrometer into the soil. We may therefore expect to measure comparable pressures to CPT measurements in coarse grained material like sand but higher pressures in finer grained materials.

3.3. Laboratory copy of the Huygens penetrometer (ACC-E)

A copy of the Huygens ACC-E penetrometer (figure 7) is used to make measurements in similar targets to X-PEN. The ACC-E penetrometer measures force during penetration using a piezoelectric sensor housed behind a hemispherical tip (Lorenz et al., 1994). It is well characterised and therefore well suited to validating penetrometry measurements made by X-PEN. It is the same penetrometer used during laboratory tests to help interpret results from the Huygens landing on Titan and reported in Zarnecki et al. (2005); Paton (2005).

3.4. Target containers, materials and target preparation

Table 2 lists the properties of the analogue regolith materials used for our experiments. Sand was chosen as an analogue regolith as it is a well known material and reproduces some of the expected properties of planetary regoliths such as granularity, porosity and composition. Figure 8 shows a close-up image of the sand in which rounded grains can be resolved. Well rounded grains on Earth can be created by saltation actions during their transportation along a river. Such rounded particles may be expected to be found on Mars, e.g., (Goetz et al.), which experiences aeolion weathering, or Titan which experiences similar weathering processes to that on Earth. In this respect sand does not reproduce angular particles found in the airless regoliths of the Moon and expected on asteroids.

To simulate the particle angularity found in an airless regolith we used iron powder and limestone powder. Iron powder has a very rough surface similar to particles found in the lunar regolith (McKay et al., 1991). Limestone powder is angular and has a fine particle size similar to the top layers of the lunar regolith or possibly the dusty surface of a comet, e.g., Kearsley et al. (2008). Figure 8 shows images of the grains for each of these materials.

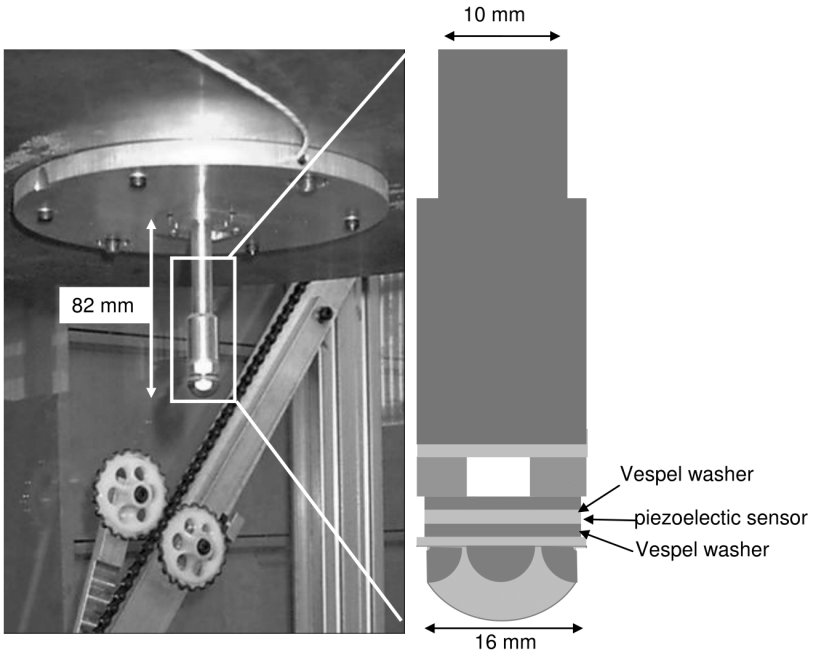

Figure 7: Huygens ACC-E penetrometer and adaptor plate attached to the underside of the test rig base plate. In the background is a section of the chain.

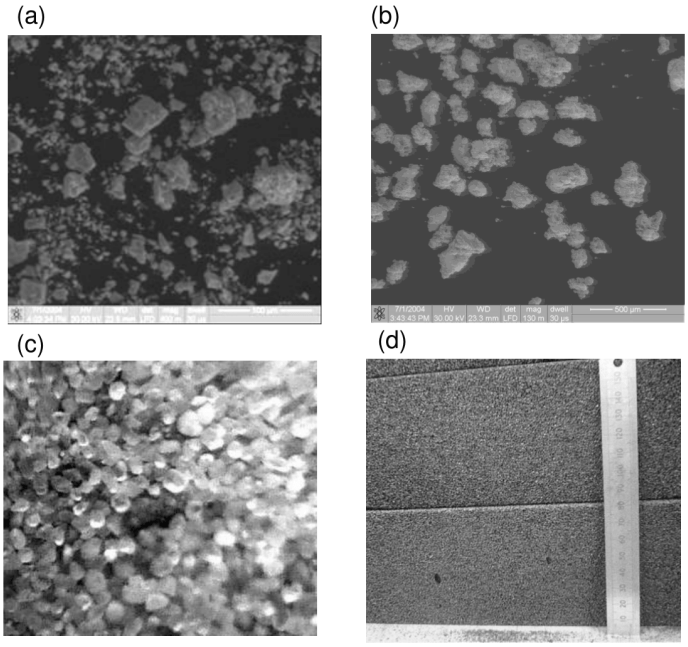

Figure 8: Details of target materials used for the penetrometry tests (Paton, 2005; Paton et al., 2012b): (a) limestone powder; (b) iron grains; (c) sand; (d) foamglass.. The properties of the granular materials can be found in table 2.

A measure of how strongly a material resists compaction can be quantified using the volumetric strength, σ_v, and the compaction energy, E_c. The volumetric strength measures the target's ability to resist penetration from an impacting object. The compaction energy is a measure of how easy it is to compact the target by shaking. A higher number indicates that more energy is required to compact the material by a given volume when starting from its loosest state. Values of σ_v and E_c are listed in table 2 for each material.

An important property, when considering which regolith analogues to use, is the bulk density, ρ. The bulk density of a granular material is linearly proportional to their solid grain density and porosity. The density of planetary materials can vary from extremes of 1 to almost 8 g cm^{-3} for water ice and iron meteorites respectively.

If the bulk density and solid density are known then the porosity can be calculated. The porosity is good for guaging the compaction state of a granular material. Porosity can vary from 0.5 for loose fluffy material to around 0.26 for highly compacted material. The lunar regolith decreases from 0.52 at the surface to about 0.46 at a depth of 60 cm (Carrier et al., 1991). The surface porosity of asteroids has been determined to be about 0.5 at depths of a metre or more using radar.

Table 2: Analogue planetary regolith properties where θ_r is the angle of repose, Y is the sphericity, ρ_0 is the bulk density when poured, σ is the volumetric strength and E_c is the shake energy required to compact and reduce the target volume by 1%. The uncertainty on the angle of repose and bulk density are due to measurement uncertainty. Details of these properties and their measurement can be found in Paton (2005).

Property	*Sand*	*Limestone powder*	*Iron powder*
d (μm)	200	1-10	10-200
θ_r	28° ± 1 ‘	50° ± 1	42° ± 1
Y	0.95 ± 0.10	0.86 ± 0.11	0.79 ± 0.10
R	0.55 ± 0.01	0.25 ± 0.03	0.16 ± 0.01
ρ_0 (g cm^{-3})	1.29 ± 0.03	0.94 ± 0.03	2.71 ± 0.06
ρ_s (g cm^{-3})	2.5	2.3-2.7	7.9
σ_v (kPa)	170 ± 12	11 ± 1	178 ± 13
E_c (J)	7	3	10

A small container, a regular plastic garden bucket was used, for testing the penetrometers sensitivity to target compaction states, as it allowed relatively

rapid preparation of numerous granular targets. The target was prepared using a tapping technique described in Paton (2005) that involved controlled impacts of the bucket base with the ground. The method allowed the repeatable preperation of target compaction states. Limestone powder, block paving sand and iron powder were used to test the penetrometer's sensitivity to target compaction.

A consolidated planetary surface was simulated using foamglas which is shown in figure 8. Foamglas makes a good analogue for a cometary crust and is a well characterised matarial. It has been used by previous workers for penetrator tests (Kömle et al., 1997; Lorenz & Shandera, 2002). The strength of foamglas is around 2 MPa which is of the same order as the strength of a crust produced during comet crust simulations (Kochan et al., 1989a). Foamglas also provides a highly reproducible target enabling measurements from X-PEN to be reliably compared with the well characterised copy of the Huygens ACC-E penetrometer.

Investigation of speed dependent pressure effects required a larger container to accomadate the higher impact speeds and greater penetration depths. A large container was also required to minimise boundary effects e.g. see (Landry et al., 2003). To hold the target a large steel bucket was used with a diameter of 50 cm and a height of 60 cm. Sand was used as the target material as it is well characterised and was available in large quantities.

With such a large and heavy target it is not possible to prepare repeatable targets using a tapping technique so an alternative technique had to be developed. The sand target was loosened for the first test by stirring using a long pole. The target was then prepared for the next impact by withdrawing the penetrometer allowing sand to pour into the cavity left by the penetrometer as shown in figure 9. This then allowed a repeatable preparation of the target which was required for investigating speed related effects. The target was assumed to fail along the slip lines as shown in figure 9 by dilation (Puech & Foray, 2002) and therefore no significant compaction of the material over time was expected.

4. Forces on the penetrometer tip

The pressure on the penetrometer tip can be represented by the following formula which is a general mathematical description of a hard penetrator travelling through a softer solid material (Allen et al., 1957) and includes

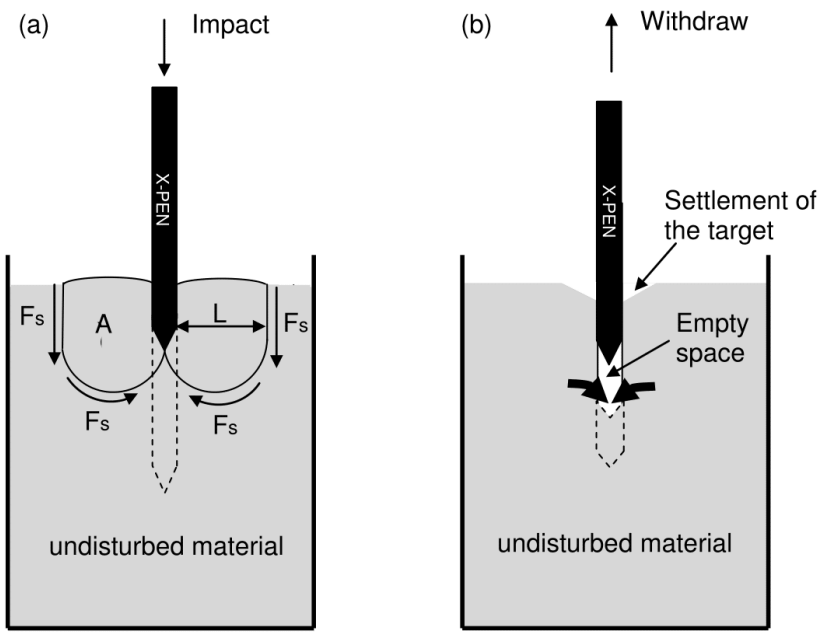

Figure 9: Deformation of the target due to the insertion and withdrawal of a penetrometer. During insertion (a) the material shears along slip line as the material is pushed out of the way. During withdrawal the material falls back into the cavity left by the penetrometer.

both static and dynamic components of the pressures on the penetrating object.

$$P_{pen} = \alpha v^2 + \beta v + \gamma \tag{1}$$

where v is the speed and the coefficients α, β and γ may be functions of space and time. The first term represents momentum transfer between the penetrometer and the target. The second term represents the viscosity and the third term represents the strength. When the tip is completely immersed in the target the dynamic pressure term has the following general form found in fluid dynamics.

$$\alpha = 0.5 C_D \rho v^2 \tag{2}$$

where C_D is a drag coefficient analogous to that used in fluid dynamics and ρ is the bulk density. For examples of explicit definitions of the drag coefficient see Kömle et al. (1997) and Johnson (2003).

The second term is analogous to viscosity and is a force acting parallel to the surface of the penetrator. The presence of this force is under debate as it is not clear whether this force is required to obtain a good fit of the model to measurements. We will ignore this term.

The last term represents the strength of the material. In a granular material such as sand the material will fail along slip lines generating shearing forces which are proportional to the constraining force on the shearing plane due to the weight of material above it.

A soil with cohesion between the grains can be modelled with an additional constant strength term, c. Strength may be due to bonding between the grains or electrostatic force. Typical values of cohesion for lunar regolith are the order of 1 kPa and have been attributed to van der Waals forces, e.g., (Rozitis et al., 2014). On Earth the cohesion between grains is smaller (Perko et al., 1996). A purely cohesive model, i.e. $\gamma = c$, is applicable to a material with a cell-like structure such as foamglas (Kömle et al., 1997).

For a conical penetrometer in medium to dense sand the resistance to penetration due to slip-line failure in sand can be expressed as follows, e.g. Puech & Foray (2002) which we will refer to as model A.

$$\gamma_A = N_A \rho g z (1 + K sin\phi_A D/L) \tag{3}$$

where ρ is the bulk density, ϕ_A is the effective friction angle of sand, z is the depth of the tip of the cone, g is the gravitation acceleration and D is

the diameter of the penetrometer. The friction factor, K, governs the forces between the disturbed zone and the target at rest. A value of $K = 0.7$ was found empirically by Puech & Foray (2002) through a curve fitting procedure to multiple CPT soundings in sand. The the lateral extension of the slip lines, L, can be expressed as follows.

$$L = Be^{\frac{\pi}{2}tan\phi_A}tan\left(\frac{\pi}{4} + \frac{\phi_A}{2}\right) \tag{4}$$

Where B is the cone diameter. The value of the Terzaghi coefficient, N_A, calculated under asymmetric conditions can be approximated by the following equation.

$$N_A = 1.0584e^{6.1679tan\phi_A} \tag{5}$$

Another model that has been used by various workers studying the forces on penetrators (Anderson et al., 1996; Kömle et al., 1997) is to integrate the forces, due to the inertial processes and mechanical strength, over the wetted area of the penetrator cone to find the resistance force of the target. Such a model requires such parameters as the cone half angle and sliding friction between the target and the wetted surface of the cone. This model is updated by Kömle et al. (2001a) to include viscosity, overburden and gravity terms and presented in their paper as an integral. A final, derived equation of the overburden term can be found in Paton (2005). The velocity terms are ignored as the experiments are conducted at low velocity. The equation is repeated here as follows and we will refer to this as model B.

$$F_{\gamma_B} = 2\pi N_B \rho g \frac{tan\theta}{cos\theta}\left(sin\theta + \mu_f cos\theta\right)\left(\frac{zh_{cone}^2}{2} - \frac{h_{cone}^3}{3}\right) \tag{6}$$

where θ is the half angle of the penetrometer cone, μ_f is the coefficient of sliding friction, h_{cone} is the height of the tip. Here we convert the force into a pressure, as calculated in equation 3, so the two equations can be compared easily. Dividing equation 6 by the cross-sectional area of the penetrometer cone, $A_{base} = \pi h_{cone}^2 tan^2\theta$ we have.

$$\gamma_B = N_B \rho g\left(1 + \frac{\mu_f}{tan\theta}\right)\left(z - \frac{2h_{cone}}{3}\right) \tag{7}$$

The coefficient N_B, derived from the bearing capacity equation, is as follows.

$$N_B = e^{\pi tan\phi_B} tan^2 \left(\frac{\pi}{4} - \frac{\phi_B}{2} \right) \quad (8)$$

where ϕ_B is the friction angle for the target using equation 7.

5. Results

Experiments to investigate the impact penetrometer's performance were made in loose granular targets, in a consolidated rock-like or ice-like analogue and in sand at different speeds and the results are presented here. The penetrometer measurements are plotted against depth measurements made by the shaft encoder. This is to enable the fitting of a penetration model to the data, which is then used in section 6 to assess the results. Table 3 summarises the details of the experiments the results of which are reported in this section and section 6.

Table 3: Summary of experiments.

Experiment	Target material	Container	Gravity	X-PEN	ACC-E	fig.
Compaction	Sand	Small	Asteroid	X		10
Compaction	Iron powder	Small	Asteroid	X		10
Compaction	Limestone powder	Small	Asteroid	X		10
Compaction	Sand	Small	Asteroid		X	10
Hard target	Foamglas	none	Asteroid	X		13
Hard target	Foamglas	none	Asteroid		X	13
Speed	Sand	Large	Asteroid	X		16
Speed	Sand	Large	Titan	X		17
Speed	Sand	Large	Titan		X	18

5.1. Tests in loose and compacted targets

Penetrometry results of pressure against depth are displayed in figures 10 (a) to figure 10 (d). The pressure was measured using the load cell in the penetrometer. The distance was determined using the shaft encoder. Equations 6 and 8, i.e. models A and B, were used to determine the friction

angles, ϕ_A and ϕ_B and the results are listed in table 3 and are discussed in the following sections.

Figure 10 (a) shows measurements by X-PEN in limestone powder. The compacted target can be clearly distinguished from the loose target. In both the loose and compacted target the pressure is below the resolution of the penetrometer during penetration of the top layers. It then rises exponentially with depth, near the bottom of its container for both loose and compacted targets. An even sharper rise in pressure is experienced by X-PEN as the tip makes contact with the floor of the container. Three impacts were each made into the loose and compacted limestone targets.

A limited number of impact tests were made in iron powder as the target had a high density and was problematic to handle. One test was made in a loose target and one test in a compact target at low speed. These are shown in figure 10 (b). A high speed test was also made into a loose iron powder target. High speed tests were possible in iron powder, but not the other targets, because iron powder stops the penetrometer before it penetrates the floor of the container. The measurements in iron powder also appear to exhibit an exponential-like increase in pressure with depth. Measurements into the compacted target are clearly distinguishable from measurements into the loose target.

Impact tests into sand are shown in figure 10 (c) using X-PEN. The pressure dependence on depth exhibits a slightly more complex variation than for limestone and iron powder. Figure 10 (d) showing measurements in sand by ACC-E shows a similar variation in pressure with depth. Again the measurements in the compacted target are clearly distinguishable from the measurements into the loose target.

The corresponding measurements of speed are shown in figure 11. These were derived from the test rig's shaft encoder and obtained in parallel with the penetrometer pressure measurements (figure 10). For clarity only two examples are shown in figure 11 (a) during impacts into limestone powder. Note the constant speed during the penetration of the smaller ACC-E penetrometer in both compact and very compacted sand. The steep decrease in speed in figure 11 (b) is due to the impact of the baseplate with the sand. In very compacted sand the decrease in speed is steeper than in compacted sand as one would expect.

Figure 12 shows photographs of a twin thermal probe that was developed in Paton et al. (2012b). This is shown because the penetrometry experiments with X-PEN were not documented in this way. The dimensions for the

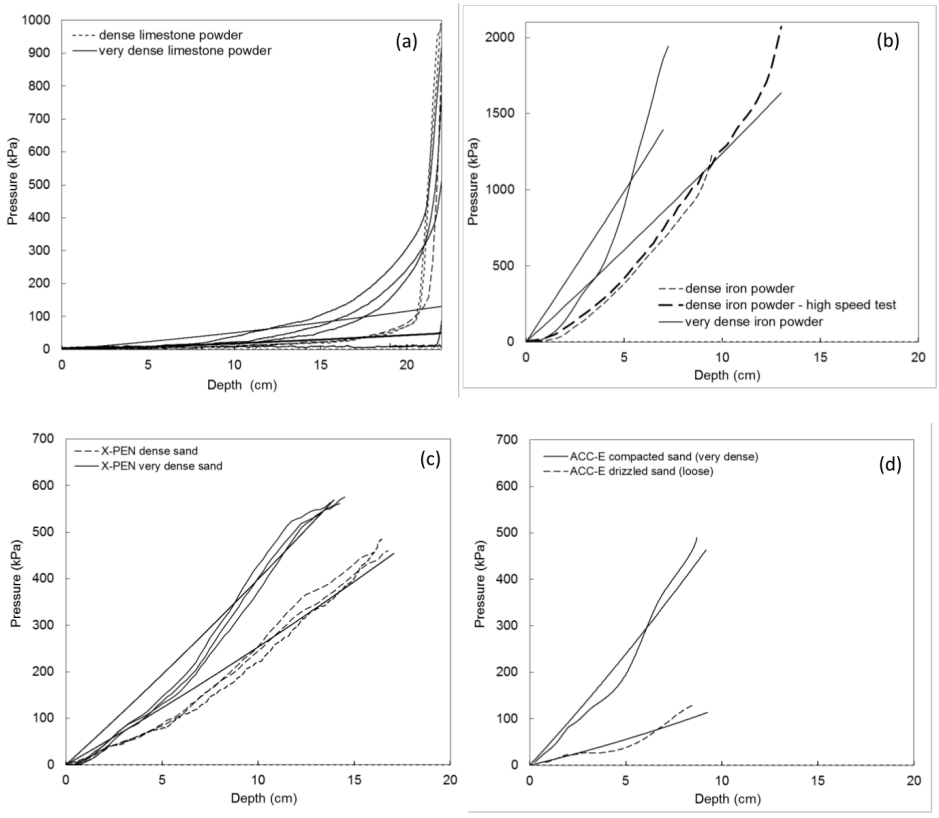

Figure 10: Penetrometry measurements into loose and compacted materials together with best fits of equation 3. The pressure measurements were made by X-PEN. Speed measurements were made simulataneously by the shaft encoder and the results are shown in the next figure. The figures show penetrometry in (a) limestone powder by X-PEN, (b) iron powder by X-PEN, (c) sand by X-PEN and (d) sand by ACC-E. The impact speed for all impacts is about 0.9 m s^{-1}

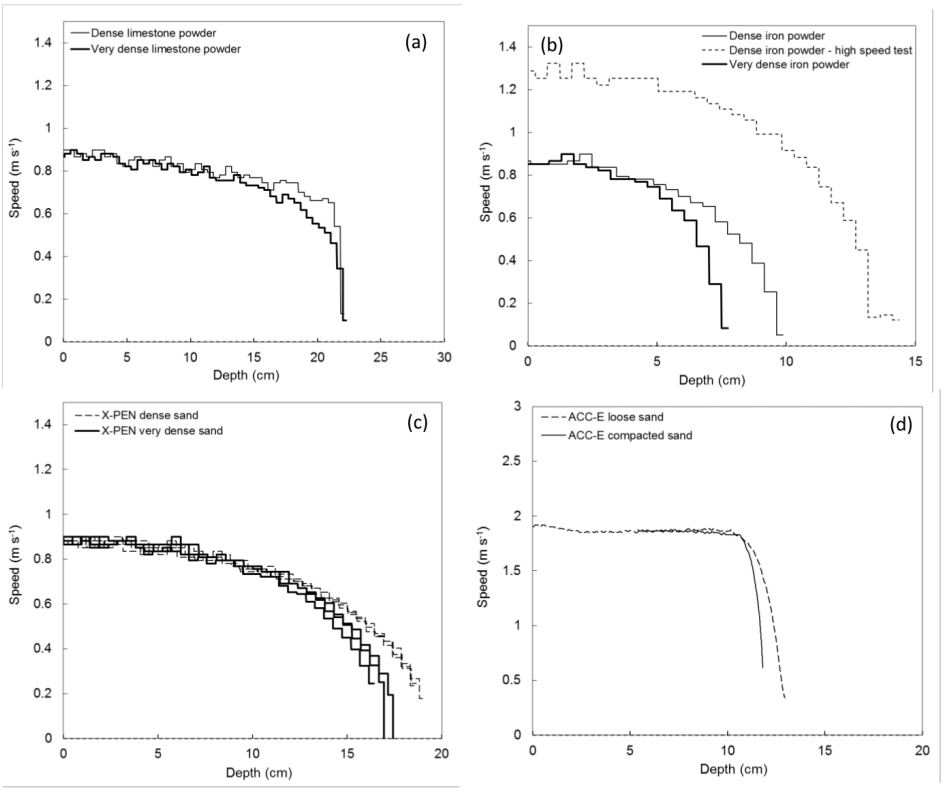

Figure 11: Speed measurements in loose and compacted materials made by the shaft encoder. Also shown is the start of penetration determined using an accelerometer. The figures show the results for impacts into (a) limestone powder by X-PEN, (b) iron powder by X-PEN, (c) sand by X-PEN and (d) sand by ACC-E.

thermal probe are the same as for X-PEN. The impact speed was the same for both the thermal probe and X-PEN experiments so the disturbance of the material can be considered representative of that caused by the experimental penetrometer X-PEN.

5.2. Measurements in a comet crust analogue

Three impacts into foamglas were made with X-PEN. Two of the measurements are shown in figure 13 (a). The third impact resulted in the splitting of the target and is not shown here as the measurement was corrupted. One impact into foamglas by ACC-E was also made and is shown in figure 13 (b). Both penetrometers measure a steep rise in pressure, over a depth of a few centimetres and reach a maximum pressure of about 2 MPa. ACC-E penetrated further than X-PEN into the target due to its smaller cross-sectional area and observed a slightly decreasing pressure with depth.

The impact of the test rig base plate during the test with ACC-E is clearly apparent in the shaft encoder measurements with a rapid decrease in speed at a penetration depth of 9 cm. The emergence of the tip of ACC-E through the bottom of the foamglas block is indicated by a drop in pressure at a depth just before the base plate impact. The magnitude of the pressure on the tip of both penetrometers correpsond with the strength of foamglas.

Post-penetration photographs of the tests with X-PEN are shown in figure 14. A direct measurement of penetration depth was made, by marking the target surface on the shaft with tape, and then measuring the distance between the removed penetrometer tip and the tape. The depth of the cavity in figure 14 (b) was also measured. Both direct measurements correspond well with each other and the distance measured by the shaft encoder.

5.3. Speed tests in sand

Penetrometer tests over a range of impact speeds in sand were made to identify any dynamic effects and whether they are significant. Figure 15 shows the results of successive impacts into the same target. A crater was created during the settlement of the target as the penetrometer was withdrawn. The depth of the crater increased with successive impacts which is reflected in the increasing depth of the penetrometer impact point as shown in figure 15. The dimensions of the final crater, as measured by a ruler, had a depth of 9 ± 0.5 cm and a diameter of 25 ± 0.5 cm, where the measurement uncertainty was mostly due to movement of sand during measurement.

(a)

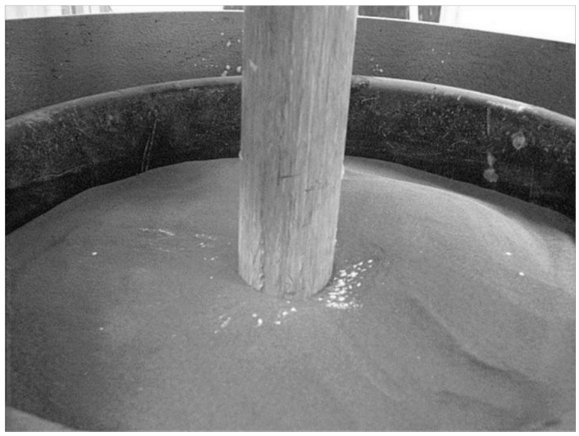

(b)

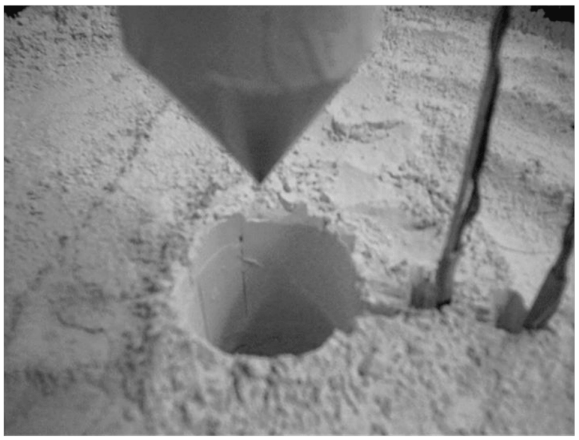

Figure 12: Images after impacts into iron powder and limestone powder using a thermal probe that is identical to the penetrometer apart from the use of a low conductivity material for the shaft and the use of a dummy load cell. The top image (a) shows significant upheaval of material due presumably due to iron powder's resistance to compaction and the bottom image (b) shows compaction around the shaft in limestone powder.

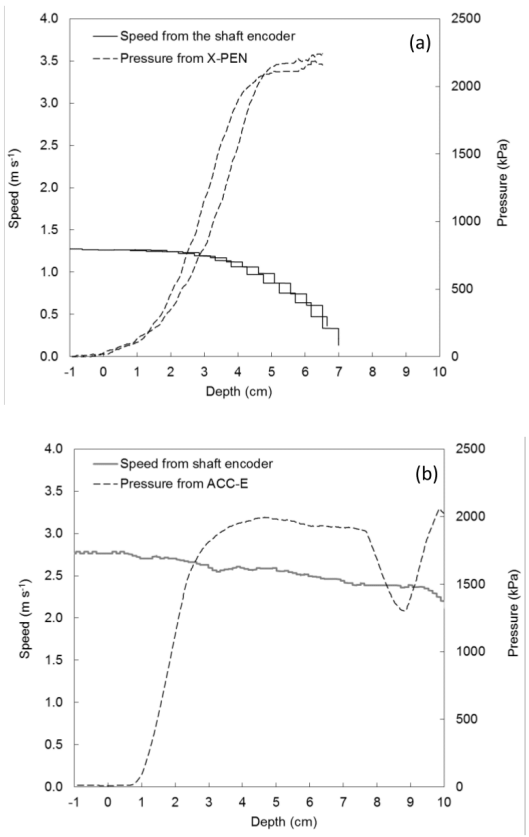

Figure 13: Speed and pressure measurements during impacts into foamglas by (a) X-PEN and (b) ACC-E.

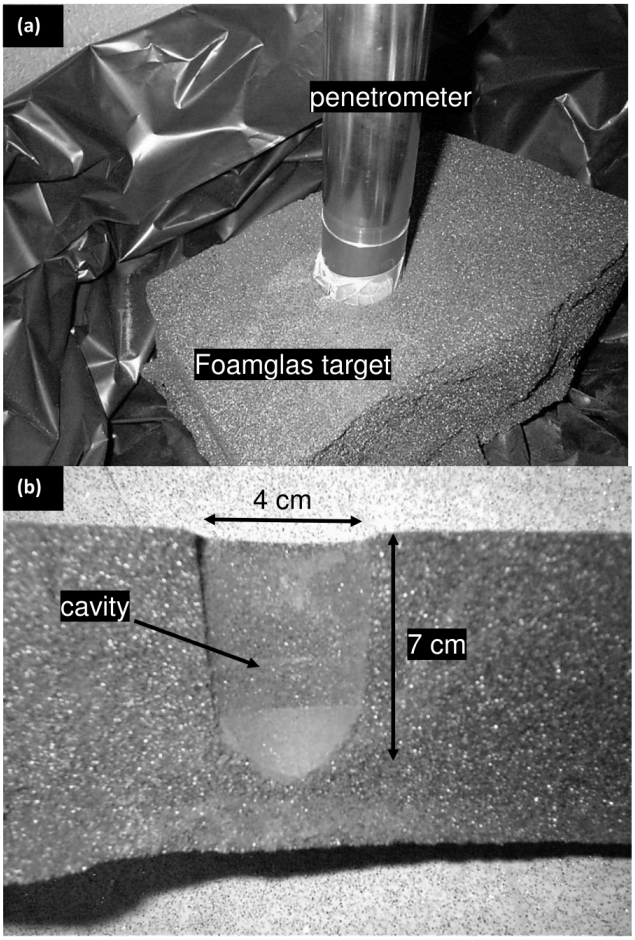

Figure 14: Photograph after impact of foamglas by X-PEN. Image (a) shows the tip of the penetrometer buried in the target. The tape wrapped around the shaft is for marking the surface location relative to the tip to determine the depth of penetration once the penetrometer has been removed. Image (b) shows the foamglas target split open to reveal the cavity, which can also be used to determine the depth of penetration.

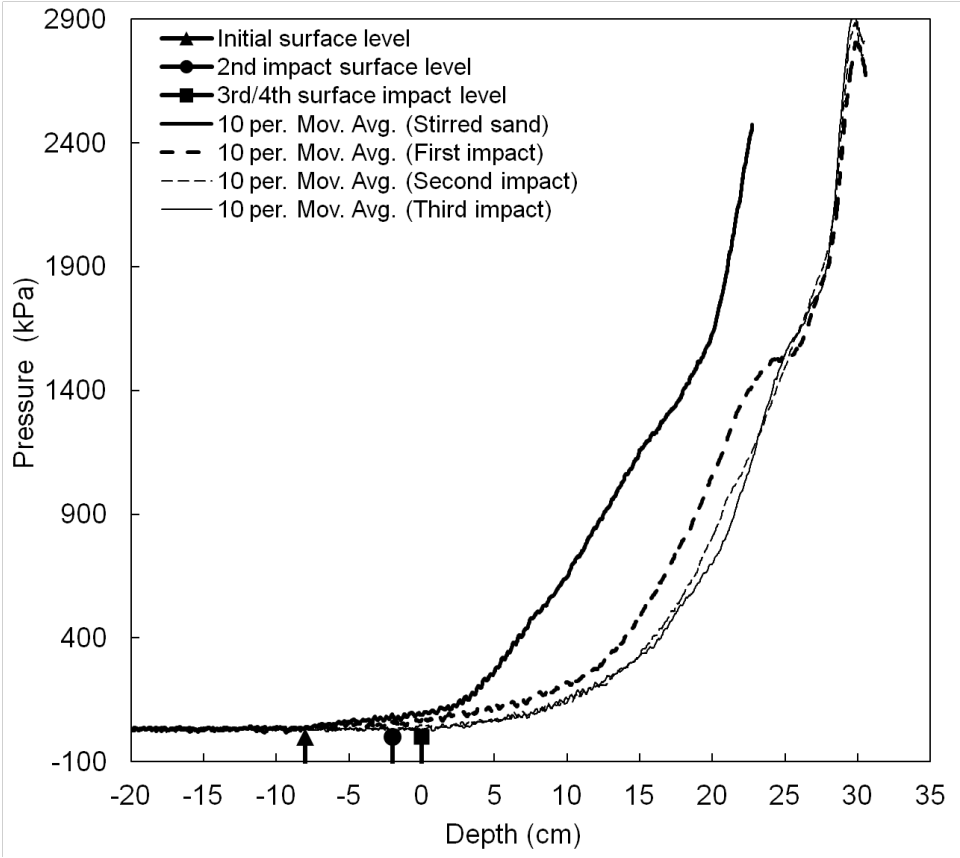

Figure 15: Settlement of the target due to repeated impacts into the same target. The pressure profile evolves with each subsequent drop. The surface of the target becomes lower due to the formation of a crater when the penetrometer is withdrawn. The surface of the target eventually stops descending as indicated by the last two drops.

A distinct evolution of the profiles can be seen in figure 15 following each impact. Subsequent impact profiles appear to be a blend of the more distinct sections in the previous profiles sections. This eventually results in a smoothly increasing pressure with depth.

Figures 16 and 17 show penetrometer pressure measurements from two sets of drop tests into sand. One set was with the rig configured for simulating landings on asteroids and the other set used the rig configured for simulating landings on Titan. Each set contains drop tests made at different impact speeds. The drop tests began by using the lowest impact speed increasing the impact speed for subsequent tests until the fourth test which used the highest impact speed. The process was repeated three times for each impact speed to gain some understanding of the variance and if any further compaction occurs.

There are several features observed that are common to both figures 16 and 17. These include a gradually steepening gradient similar to that seen in figure 15 and the appearance of a bump like feature towards the end of penetration which has a curious evolution with impact speed. Right at the end of penetration some small oscillations appear. These are due to the averaging of the step-wise distance derived from the shaft encoder data to obtain a smoothly varying distance. Towards the end of penetration, when the penetrometer is moving slowly, the constant moving average window does not successfully smooth the large step changes in distance with time.

Measurements made by ACC-E at different speeds in sand are shown in figure 18 with (a) showing the pressure during penetration of ACC-E and (b) showing the same plus the pressure during impact and penetration of the base plate. In figure 18 (a) the general trend for each test includes a constant pressure phase during penetration of the first few centimetres followed be an exponential rise in pressure during the following few centimetres of penetration. In figure 18 (b) there is a steep rise in pressure that corresponds to the impact of the test rig base plate. The measurements by ACC-E are similar in magnitude to those made by X-PEN in sand in the first 8 cm.

6. Assessment of penetrometry results

To assess the compaction and disturbance of the material around the penetrometer we examine the results quantitatively and qualitatively in terms of penetration models and processes known to occur in granular materials in response to a penetrating object.

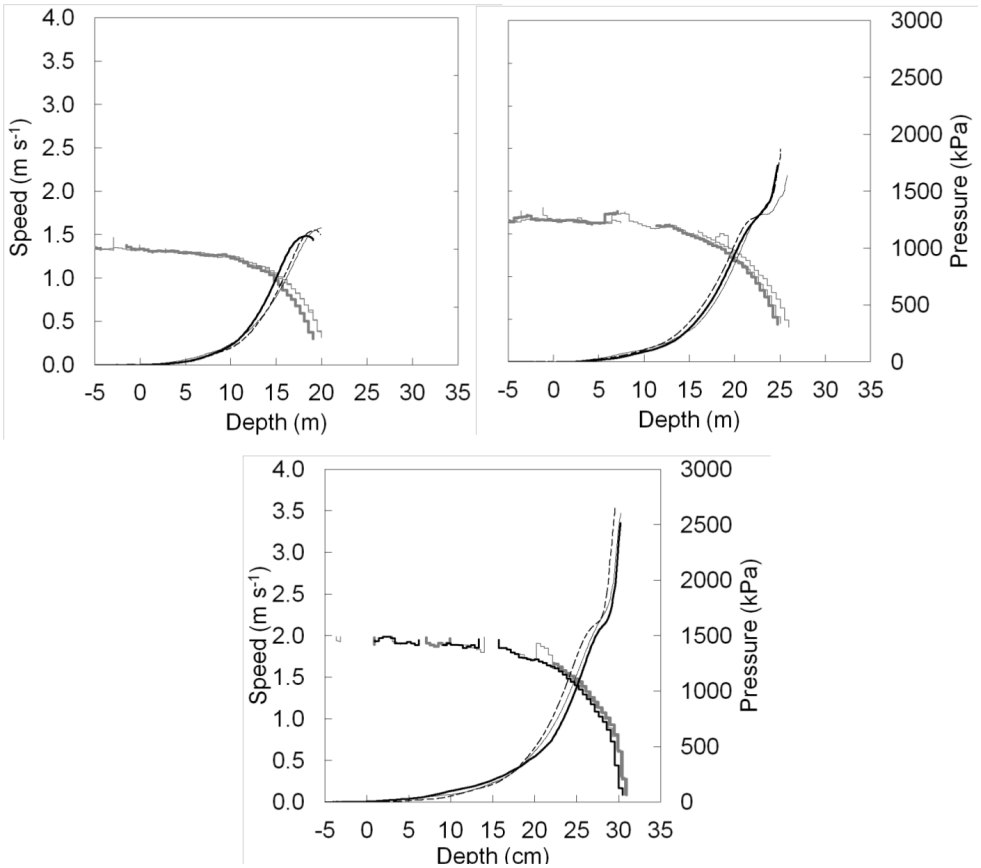

Figure 16: Penetrometer measurements in sand with the test rig configured to simulate landings on an asteroid at different speeds which are 1.3, 1.7 and 2.0 m s^{-1}. The pressure measurements were made by X-PEN. The shaft encoder data was used to determine the speed of the penetrometer during penetration as shown. At each impact speed three drop tests were made assess repeatability.

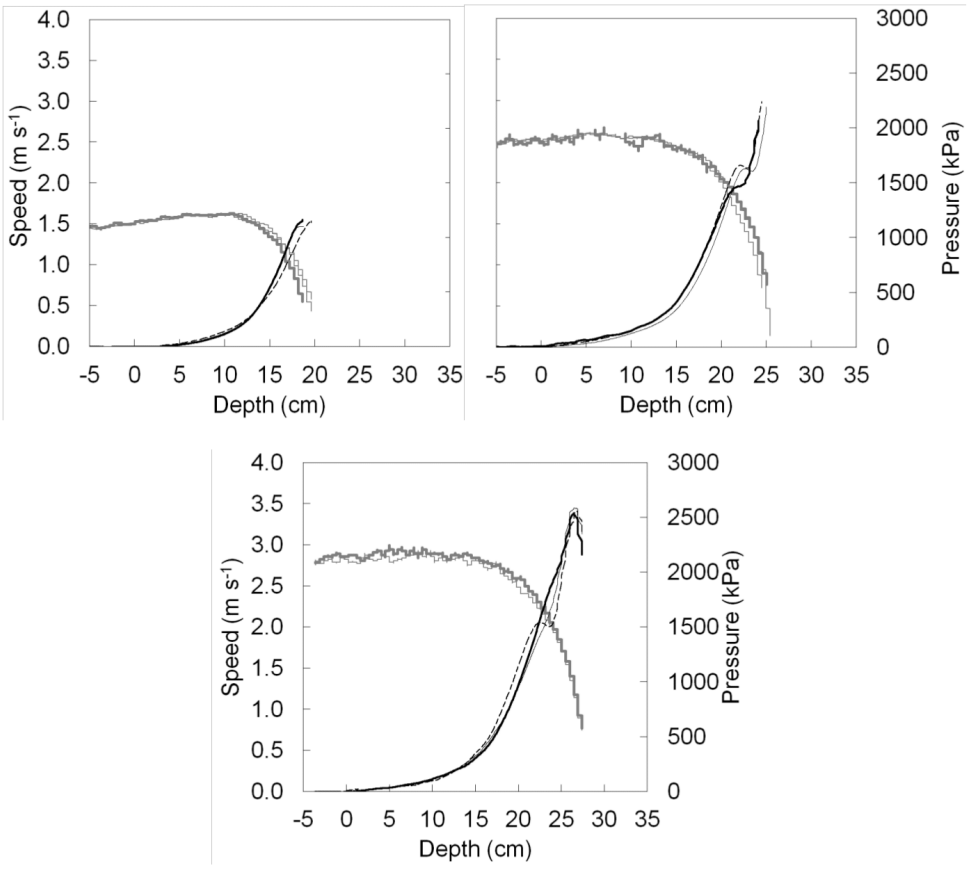

Figure 17: Penetrometer measurements with the test rig configured to simulate landings on Titan into sand at different speeds which were 1.7, 2.5 and 2.9 m s^{-1}. The pressure measurements were made by X-PEN. The shaft encoder data was used to determine the speed of the penetrometer during penetration as shown. At each impact speed three drop tests were made. Notice here the speed increases for a short while after penetration of the tip due to the larger simulated gravitational acceleration than in figure 16.

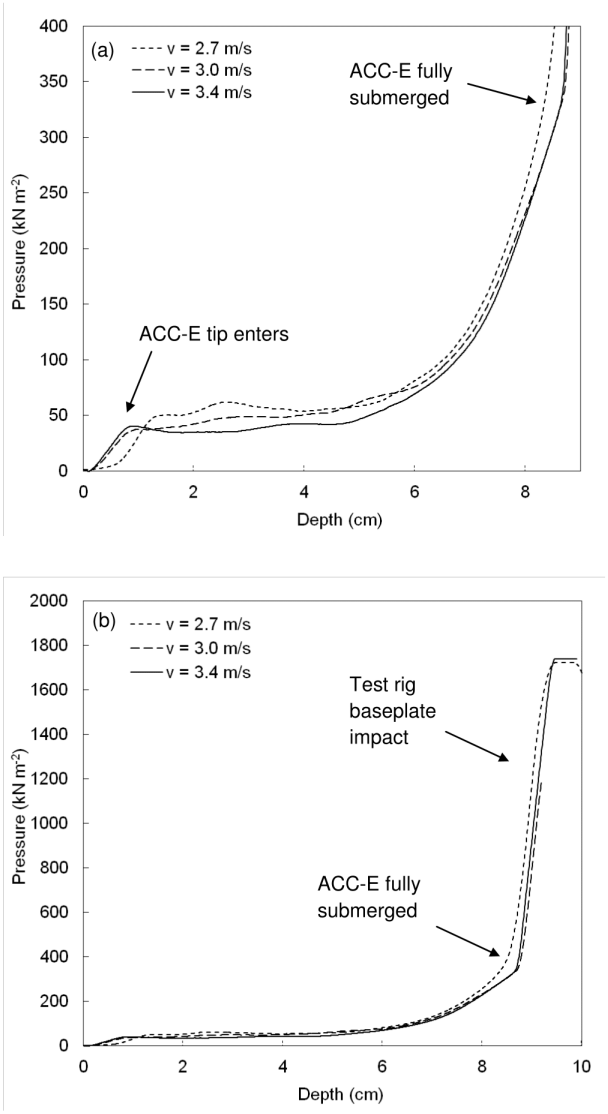

Figure 18: Penetrometer measurements with ACC-E at different speeds into a compacted target. Repeated drops into the same sand target were made letting the base plate compact the surface. The top figure (a) shows the pressure during the penetration of ACC-E while the bottom figure (b) shows the penetration of the base plate as well and the much larger pressures felt by ACC-E.

6.1. Tests in loose and compacted regolith analogues

The friction angle is very sensitive to the compaction and can be related to the relative density (Puech & Foray, 2002). We will examine the friction angle here to characterise the materials impacted by the experimental cone penetrometer (X-PEN). The effective friction angles shown in table 4 are obtained from the fit of the models to the measurements. They are in general agreement with each other except for limestone powder. This is due to the slightly different formulae that represent the models. The difference between the models becomes more noticeable in looser material because low friction angles are less sensitive, for a given change in gradient or pressure against depth, than for higher friction angles. In compacted materials the friction angle varies less with changes in the gradient of pressure with depth.

Table 4: Results from fitting models A and B to the penetrometry measurements. The parameters, ϕ_A, N_A, ϕ_B, N_B listed below were obtained using a least squares fit of Model A to the measurements as shown in figure 10 and model B was fitted likewise in Paton (2005). The density, ρ was determined from laboratory measurements. The cone angle used was $\theta = 30°$. The coefficient of lateral pressure was $K = 0.7$. The friction coefficient, $\mu_f = 0.3$ which is representative of sand grains passing over a metal surface. The uncertainty on the friction angle determined from the models is about $\pm 0.1°$.

Material	ρ (kg m^{-3})	ϕ_A (deg.)	N_A	ϕ_B (deg.)	N_B
loose limestone	1.03	20.7	10.9	25.2	18.2
compact limestone	1.09	28.9	31.8	33.7	49.1
loose iron	3.00	43.9	400	45.0	252
compact iron	3.10	46.2	657	46.0	300
loose sand	1.38	39.5	171	37.5	83.3
dense sand	1.42	42.0	273	41.0	134

The friction angles for limestone powder, listed in table 4, correlate well with loose and compacted targets. Limestone powder is easy to compact when handled in the laboratory and that seems to be reflected in the large change in measured friction angles. Sand does not exhibit such a large change in friction angle. Iron powder even less. A reason for the different levels of compaction can be explained by the microstructural properties of the target. Limestone powder appears easy to compact because it contains both large and small particles. The small particles can occupy the spaces between the large particles. Sand, when prepared in its loosest state, is the most compact

of all the materials because its grains are rounded and can slip past each other easier into a more compact state. Iron powder begins relatively porous but does not compact well because its grains are very rough and angular and so resist compaction.

When comparing the results from the two models, the friction angles are in relatively good agreement for iron powder and sand which suggests both equations are at least well 'designed' for predicting the pressures in these materials. The friction angles for limestone powder obtained using model A are significantly lower than for the friction angles obtained from model B. This is possibly due to the use of bearing capacity coefficient derived from using different slip line analysis techniques. The different techniques can produce very different values for their coefficients, e.g., see Gui & Muhunthan (2006) for a detailed analysis using the axi-symmetric slip line approach.

Comparison of the friction angle to the angle of repose (see table 2) can provide information regarding relative density. The friction angle of a granular material in its loosest state is closely related to the angle of repose. For a non-cohesive granular material the angle of repose is normally less than the friction angle.

The change in friction angles of sand and iron powder are in agreement with this behaviour. Iron powder has the closest agreement between measured internal angle of friction and the angle of repose. This is likely because iron powder is difficult to compact (Paton, 2005) and is in a relatively loose state close to the state of compaction at which the angle of repose was measured. The measured friction angle for limestone is much lower than its angle of repose. A high angle of repose could be explained by a significant amount of cohesion between grains. Limestone powder can clump together and if compressed vertical walls can be made. The relatively low friction angle, predicted by both models in table 4, compared to the angle of repose may reflect a different mode of failure in limestone powder than in sand and iron powder. Sand fails due to shearing along slip lines. For limestone powder it appears that compaction is the dominant mode of failure which is a process perhaps not captured properly by the models used here.

The dependence of pressure on depth is closer to a linear relationship for iron powder and sand, compared to limestone powder. This suggests these targets do not increase in compaction so much with depth and are less sensitive to self-compaction during preparation. During impacts into limestone powder the pressure rises exponentially with depth, near the bottom of its container. This could be explained by increased compaction in the target

with depth due to the weight of material above. It was found by Paton (2005) that when emptying a limestone powder sample from the bucket the material became much stiffer towards the bottom. Limestone powder is a weak material and is less effective at supporting itself against gravity than sand and iron powder in its loosest state.

Another reason for the increasing pressure near the bottom of the bucket in limestone powder could be due to confinement in a container with boundaries. Bolton & Gui (1993) investigated boundary effects using a cone penetrometer in sand. They placed a pressure sensor at the bottom of a container. Almost as soon as the penetrometer entered an increase in stress was measured. This was at a depth of 30 times the diameter of the penetrometer.

The steep, almost vertical increase in pressure observed in limestone powder at a depth of around 20 cm is due to the tip striking the floor of the sample container. It was found after tests that the floor of the container was cracked.

6.2. Measurements in a cometary crust analogue

The measurements by both penetrometers in foamglas corresponded closely with each other. The small differences could perhaps be accounted for by variations in the strength of the blocks of foamglas. However measurements by ACC-E appear to be correlated to the speed measured by the shaft encoder with decreasing pressure as the speed decreases. In the X-PEN measurements there is a slight rise at the end of penetration possibly due to an increase in friction as the tip comes to rest or some other mechanism such as an increase in the drag coefficient. It is possible crushed material being pushed ahead of the tip increases the effective tip surface area of the tip and increases the friction between the tip and the surrounding material.

A number of previous workers have conducted penetrometry tests in foamglas (Lorenz & Shandera, 2002; Kömle et al., 2001a). Lorenz & Shandera (2002) observed a significant volume of crushed foamglas at the bottom of a tunnel during tests of the DS2 penetrator equal to about half the volume of the penetrators hemispherical nose. In our tests we observed a small amount of crushed material at the bottom of the hole excavated by the X-PEN penetrometer. A slight bulging in the outline of the cone can be observed in figure 15 (b) due to the accumulation of material during penetration. There is also an indication that the hole diameter decreases with depth, by a milimetre or so, which could be caused by the sloughing of material to the side and the

crushing of the material to the side. Kömle et al. (2001a) observed a crushed powdered layer in tests during laboratory tests of the Philae anchor.

6.3. Speed tests

The initial series of successive impacts by the penetrometer at high speed into sand, shown in figure 15, clearly shows the initial state and subsequent evolution of the target structure in response to the cycle of impacts and withdrawals. Equation 3 predicts that the pressure on the tip will be linearly proportional to the depth and have an exponential-like relationship with compaction. Examining figure 15 in the context of these relationships it appears the target initially had a loose layer on top, a more compacted layer beneath and an even more highly compacted layer underneath the upper layers. The very loose layer on top was most likely created during the repairing of the crater from two drop tests made during a rehearsal for the experiment. After two rehearsal drop tests the target was prepared by stirring this top layer which probably remained loose possibly because the shearing mechanism in the surface layers is due to dilation (Puech & Foray, 2002). The denser layer may be a remnant from previous drops too.

Several interesting features are apparent in figure 15. A shoulder-like bump appears in the profile from the second drop at a depth corresponding to the depth reached by the penetrometer tip during the first drop. This suggests that the bump feature may be due to the tip from the second drop passing through a compaction zone created by the first drop. Strength reduction due to dilation of locked grains could produce such a feature. Such bumps are often seen in penetrometry measurements in dense sand e.g., (ElShafie et al., 2010).

The bump feature in the second and third drops have nearly vanished probably due to the loosening of the target by the withdrawal of the penetrometer after the second drop. The blending of the distinct structure observed in the first drop measurements is likely due to the withdrawal of the penetrometer because as it is withdrawn the sand falls to fill in the cavity formed during the impact and the memory of the previous state of the target around the penetrometer is erased. The new compaction state will presumably be fairly uniform as the flow during filling of the cavity is more or less at a constant rate.

Impacts at different speeds with ACC-E into a compacted sand target, shown in figure 18 appears to show a sharp increase in the pressure during the entry of the approximately 1.6 cm diameter tip of ACC-E followed by

a region of relatively constant pressure. This can be explained if the top layer is very loose, where the steep increase is due to the rapidly increasing cross-sectional area of the tip submerged in the target. The drag coefficient, calculated from a rearranged inertial drag equation and using the measured impact speeds of 2.7, 3.0 and 3.4 m s^{-1} are 3.6, 3.0 and 2.3 respectively. The greater persistence of a compaction zone at lower speeds is a mechanism that could explain the increase in apparent drag coefficient with decreasing speed. It is also noted that the region after the tip entry decreases in pressure with increasing impact speed which could be explained by the shearing away of the compaction zone with depth.

6.4. Spacecraft g-loadings and attainable depths

To discuss the suitability of the penetrometer in terms of its performance as a landing system and an instrument two simple measures, or metrics, can be examined. These are g-loadings for examining the penetrometer as a landing system and reachable depth which describes the penetrometer's utility as an instrument. The two metrics can be related through conservation of energy. This allows the possibility of exploring and optimising the design or mission profile of the penetrometer by varying a free parameter such as impact speed.

The work done during penetration can expressed in terms of kinetic (KE) and potential energy (PE), W=KE+PE. If we assume that the pressure on the tip increases linearly with depth as in equation 3 then the maximum depth reached can be calculated as follows.

$$z_{max} = A_{X-PEN} m v_0^2 / P_{max} \tag{9}$$

where m is the spacecraft mass, v_0 is the impact speed and P_{max} is the maximum force. Figure 19 shows the maximum pressure measured by X-PEN plotted against the maximum depth for various materials. Also shown along the left-hand vertical axis is the maximum g-level loading during the impact. The maximum depth appears to be inversely proportional to the maximum pressure as modelled in equation 9. As a consequence the change in maximum depth is more sensitive to changes in the strength of the weaker materials than the stronger materials.

Also plotted in figure 19 are the results from impact tests made at higher speeds. The change in depth with change in maximum pressure appears to follow an approximately a linear relationship for sand suggesting the target

strength can be modelled using the bearing strength relationships. In a similar way iron powder such a relationship holds for the two points that were measured. More data points however would be required to rule out any speed dependence of the target response or sensitivity of the target resistance because of the confining walls of the target container.

Figure 20 plots equation 9 for a range of impact speed from 0 to 5 m s^{-1} in steps of 1 m s^{-1}. The bearing strength relationship is plotted on the same figure for the values of N_A in table 4. This then allows a preliminary assessment of reachable depths with X-PEN in different analogue regolith materials.

It is apparent from figure 20 that for a strongest material, like iron powder, that the penetrometer may penetrate its full length with a speed of perhaps <5 m s^{-1}. Such a hard surface may only occur on a small body like an asteroid or comet if there is some consolidation of the material perhaps due to sintering of grains (Kochan et al., 1989b) or high angularity of the grains (Ballouz et al., 2014). A loose granular dusty material in low gravity would be weak and easily disturbed in such an environment. For a weak material, like limestone powder, a lower impact speed (<1 m s^{-1}) will penetrate the target fully. On a real asteroid or comet such fine grained dust would lack strength due to the low specific weight of the regolith and require very slow penetration to avoid impact and compaction due to the spacecraft base plate.

7. Conclusions

Full-scale testing of a landing spacecraft fitted with an impact penetrometer was made in analogue regolith materials. Measurements were made to investigate the penetrometer sensitivity to target compaction and investigate if the strength of the targets depended on speed. The reachable depth was measured using a shaft encoder attached to the test rig and the g-loading was determined using the penetrometer force measurements and dividing by the known mass of the simulated spacecraft. A smaller, well characterised penetrometer, a copy of one flown on the Huygens mission, was used to compare with the experimental penetrometer.

The g-levels using the large penetrometer were found to be between 5 to 50 times lower than the maximum g-loading normally expected for planetary landers. The reachable depth varied from a few cm to a few 10s of centimetres.

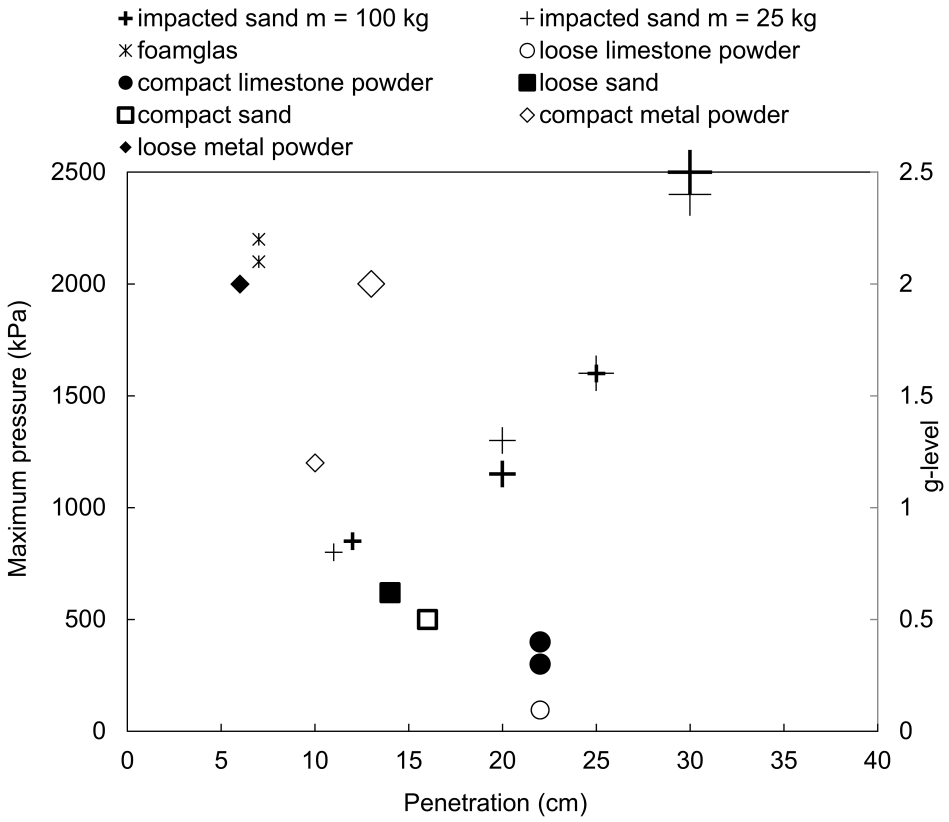

Figure 19: The maximum pressures from penetrometer tests in analogue regolith materials plotted against the corresponding depth. The bottom of the container is located at a depth of 22 cm. The limestone powder pressure measurement is close to this depth at a point just before the penetrometer motion is arrested by the impact with the container floor. The impact speed is 0.9 m s^{-1} for the low speed tests. Sand was impacted at the following speed while the rig was configured for asteroid landing: 1.3, 1.7 and 2.0 m s^{-1} and for the rig configured for landing on Titan: 1.7, 2.5 and 2.9 m s^{-1}. The higher the speed the larger of the symbol used.

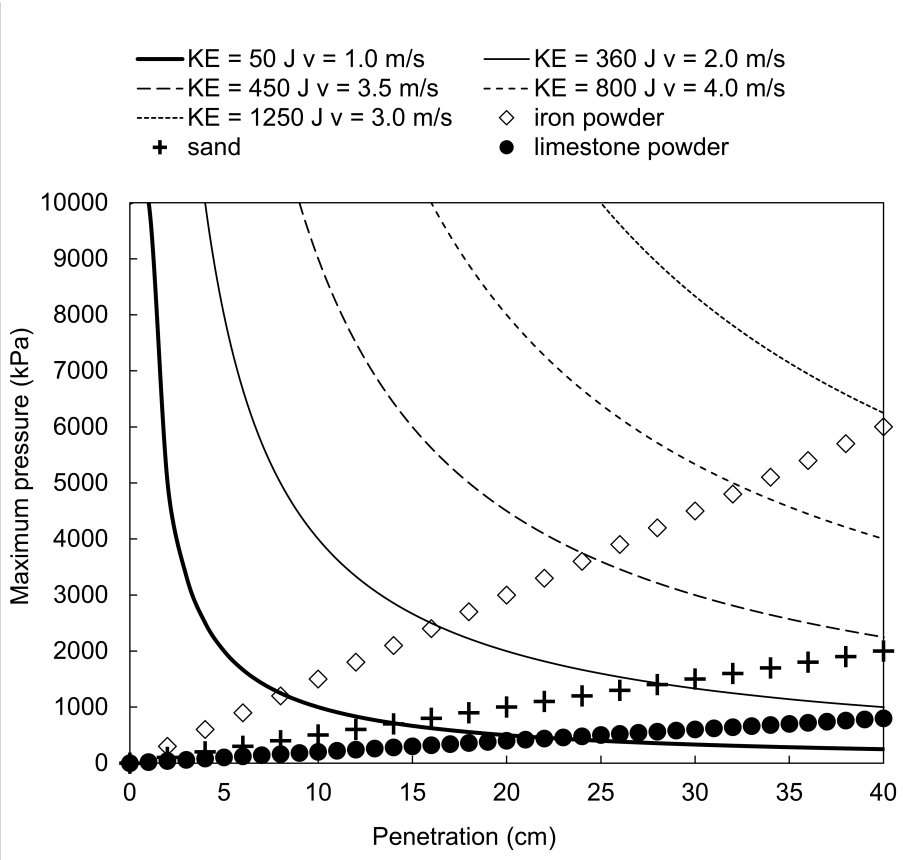

Figure 20: The equation for the static strength of the target, Equation 3, is plotted, by varying N_A, for sand and iron powder with the intercept set to zero. Equation 9 is plotted for different speeds. By examining the intercept between plots for equation 3 and equation 9 a preliminary assessment of the impact speed required to penetrate different materials can be made. The maximum pressure on the y-axis corresponds to the maximum force that can be measured by X-PEN and the maximum depth, along the x-axis, is the maximum penetration depth possible with the penetrometer.

The penetrometer, together with the shaft encoder, produced unique pressure depth profiles for the different target materials, limestone powder, iron powder and sand and was able to distinguish unambiguously between their compaction states. The friction angle was measured for all these targets and reflected their compaction states well. Tests in consolidated material demonstrated that the method of penetration could be used to penetrate hard materials such as a comet crust. The measurements by the experimental penetrometer compared favourably with a well characterised copy of the penetrometer flown on the Huygens mission.

A dependence of the pressure with speed was not resoundingly detected suggesting low speed impact penetrometer measurements in loose granular can be analysed using existing cone penetrometer theories of static penetration. Discrepencies between measurements made by two different models suggests more work is required to understand the significance of the various mechanical processes at work. A shoulder-like feature that appeared to evolve with higher impact speeds was determined to be most likely due to a shear-reduction mechanism such as dilation of locked grains. The feature was probably influenced by the proximity of the container floor to the tip.

The penetrometer delivery system outlined and tested here demonstrates itself as a promising technique for subsurface exploration of a wide range of planetary regoliths. It is particularly suited to low gravity environments. An orbiter-type spacecraft sent to an asteroid or comet, would in principle, require little modification for the attachment and deployment of the penetrometer.

Acknowledgements

The authors wish to acknowledge the Hosie Bequest to the Royal Astronomical Society that funded this work.

References

Allen, W. A., Mayfield, E. B., & Morrison, H. L. (1957). Dynamics of a Projectile Penetrating Sand. *Journal of Applied Physics*, *28*, 370–376.

Anderson, W. W., Ahrens, T. J., Gibson, A., Scott, R., & Suzuki, K. (1996). Emplacement of penetrators into planetary surfaces. *Journal of Geophysical Research*, *101*, 21137–21150.

Ball, A., Garry, J., Lorenz, R., & Kerzhanovich, V. (2010). Planetary Landers and Entry Probes. In *Planetary Landers and Entry Probes, by Andrew Ball , James Garry , Ralph Lorenz , Viktor Kerzhanovich, Cambridge, UK: Cambridge University Press, 2010*.

Ballouz, R., Richardson, D. C., Michel, P., & Schwartz, S. R. (2014). Numerical Simulations of Spacecraft-Regolith Interactions on Asteroids. In *AAS/Division for Planetary Sciences Meeting Abstracts* (p. 213.03). volume 46 of *AAS/Division for Planetary Sciences Meeting Abstracts*.

Bolton, M. D., & Gui, M. W. (1993). *The study of relative density and boundary effects for cone penetration tests in centrifuge, Report CUED/D-SOILS/TR256*. Technical Report Cambridge University, Engineering Department, UK.

Carrier, W. D., Olhoeft, G. R., & Mendell, W. (1991). Physical properties of the lunar surface. In *Lunar Sourcebook, eds.Grant H. Heiken, David T. Vaniman, Bevan M. French, Cambridge University Press, 1991*.

Coste, P., Gelmi, R., Magnani, P., Poletto, F., Schleifer, A., Perrone, A., Salonico, A., Re, E., Jollet, D., Marson, I., & Corubolo, P. (2010). "MOON-BIT" - Seismic While Drilling (SWD) laboratory testing with Lunar regolith simulant. In *12th Biennial International Conference on Engineering, Construction, and Operations in Challenging Environments; and Fourth NASA/ARO/ASCE Workshop on Granular Materials in Lunar and Martian Exploration*. American Society of Civil Engineers.

Daniels, K. (2013). Rubble-Pile Near Earth Objects: Insights from Granular Physics. In *Asteroids: Prospective Energy and Material Resources, Springer, 2013*.

ElShafie, A., Chevrier, V. F., Ulrich, R., & Roe, L. (2010). Penetration testing in Martian analog material. In *41st Lunar and Planetary Science Conference, March 1-5, Texas. LPI Contribution No. 1533*.

Gibney, E. (2014). Philae's 64 hours of comet science yield rich data. *Nature*, *515*, 319–320.

Goetz, W., Pike, W. T., Hviid, S. F., Madsen, M. B., Morris, R. V., Hecht, M. H., Staufer, U., Leer, K., Sykulska, H., Hemmig, E., Marshall, J.,

Morookian, J. M., Parrat, D., Vijendran, S., Bos, B. J., El Maarry, M. R., Keller, H. U., Kramm, R., Markiewicz, W. J., Drube, L., Blaney, D., Arvidson, R. E., Bell, J. F., Reynolds, R., Smith, P. H., Woida, P., Woida, R., & Tanner, R. (), .

Grotzinger, J. P., Crisp, J., Vasavada, A. R., Anderson, R. C., Baker, C. J., Barry, R., Blake, D. F., Conrad, P., Edgett, K. S., Ferdowski, B., Gellert, R., Gilbert, J. B., Golombek, M., Gómez-Elvira, J., Hassler, D. M., Jandura, L., Litvak, M., Mahaffy, P., Maki, J., Meyer, M., Malin, M. C., Mitrofanov, I., Simmonds, J. J., Vaniman, D., Welch, R. V., & Wiens, R. C. (2012). Mars Science Laboratory Mission and Science Investigation. *Space Science Reviews*, *170*, 5–56.

Gui, M. W., & Muhunthan, B. (2006). Bearing capacity of foundations on sand using the method of slip line. *Journal of Marine Science and Technology*, *14*, 1–14.

Hand, E. (2014). Philae probe makes bumpy touchdown on a comet. *Science*, *346*, 900–901.

Harri, A.-M., Alexashkin, S., Arrugeo, I., Schmidt, W., Vazquez, L., Genzer, M., & Haukka, H. (2014). MetNet Network Mission for Martian Atmospheric Investigations. *LPI Contributions*, *1791*, 1458.

Johnson, J. B. (2003). *A Statistical Micromechanical Theory of Cone Penetration in Granular Material*. Technical Report U.S. Army Cold Regions Research and Engineering Laboratory (CRREL), Hanover, NH.

Jones, R. H. (1971). Lunar surface mechanical properties from Surveyor data. *Journal of Geophysical Research*, *76*, 7833–7843.

Kargl, G., Kömle, N. I., Ball, A. J., & Lorenz, R. D. (2009). In *Penetrometry in the Solar System II, Graz, September 25-28, 2006, Austrian Academy of Science Press*.

Kearsley, A. T., Borg, A. A., J.and Graham, & Burchell, M. J. (2008). Dust from comet Wild 2: Interpreting particle size, shape, structure, and composition from impact features on the Stardust aluminium foils. *Meteoritics and Planetary Science*, *43*, 41–73.

Kochan, H., Roessler, K., Ratke, L., Heyl, M., Hellman, H., & Schwehm, G. (1989a). Crustal strength of different model comet materials. In *International Workshop on Physics and Mechanics of Cometary Materials, Munster*. ESA.

Kochan, H., Roessler, K., Ratke, L., Heyl, M., Hellmann, H., & Schwehm, G. (1989b). Crustal strength of different model comet materials. In J. J. Hunt, & T. D. Guyenne (Eds.), *Physics and Mechanics of Cometary Materials* (pp. 115–119). volume 302 of *ESA Special Publication*.

Kömle, N. I., Ball, A. J., Kargl, G., Keller, T., Macher, W., Thiel, M., Stöcker, J., & Rohe, C. (2001a). Impact penetrometry on a comet nucleus - interpretation of laboratory data using penetration models. *Planetary and Space Science*, *49*, 575–598.

Kömle, N. I., Ball, A. J., Kargl, G., Stöcker, J., Thiel, M., Jolly, H. S., Dziruni, M., & Zarnecki, J. C. (1997). Using the anchoring device of a comet lander to determine surface mechanical properties. *Planetary and Space Science*, *45*, 1515–1538.

Kömle, N. I., Kargl, G., Ball, A. J., & Lorenz, R. D. (2001b). In *Penetrometry in the Solar System, Graz, October 18-20, 1999, Austrian Academy of Science Press*.

Landry, J. W., Grest, G. S., Silbert, L. E., & Plimpton, S. J. (2003). Confined granular packings: Structure, stress, and forces. *Physical Review E*, *67*, 041303.

Lorenz, R., Bannister, M., Daniell, P., Krysinski, Z., Leese, M., Miller, R., Newton, G., Rabbetts, P., Willett, D., & Zarnecki, J. (1994). An impact penetrometer for a landing spacecraft. *Measurement Science and Technology*, *5*, 1033–1041.

Lorenz, R. D. (2011). Planetary penetrators: Their origins, history and future. *Advances in Space Research*, *48*, 403–431.

Lorenz, R. D., & Shandera, S. E. (2002). Target effects during penetrator emplacement: heating, triboelectric charging, and mechanical disruption. *Planetary and Space Science*, *50*, 163 – 179.

McKay, D. S., Heiken, D. S., Basu, A., Blanford, G., Simon, S., Reedy, R., French, B. M., & Papike, J. (1991). The Lunar Regolith. In *Lunar Sourcebook, eds.Grant H. Heiken, David T. Vaniman, Bevan M. French, Cambridge University Press, 1991*.

Paton, M. D. (2005). *Penetrometry of NEOs and other Solar System bodies*. Ph.D. thesis Milton Keynes.

Paton, M. D., Green, S. F., & Ball, A. J. (2012a). Microstructural penetrometry of asteroid regolith analogues and Titan's surface. *Icarus*, *220*, 787–807.

Paton, M. D., Harri, A. M., Mkinen, T., & Green, S. F. (2012b). Investigating thermal properties of gas-filled planetary regoliths using a thermal probe. *Geoscientific Instrumentation, Methods and Data Systems*, *1*, 7–21.

Paton, M. D., Kargl, G., Ball, A. J., Green, S. F., Hagermann, A., Kömle, N. I., Thiel, M., & Zarnecki, J. C. (2010). Computer modelling of a penetrator thermal sensor. *Advances in Space Research*, *46*, 337–345.

Perko, H. A., Nelson, J. D., & Sadeh, W. Z. (1996). Surface Cleanliness in Lunar Regolith Mechanics. In *Lunar and Planetary Science Conference* (p. 1019). volume 27 of *Lunar and Planetary Inst. Technical Report*.

Puech, A., & Foray, P. (2002). Refined model for interpreting shallow penetration cpts in sands. In *Proceedings of the Annual Offshore Technology Conference*. Society of Petroleum Engineers.

Rogers, J. D. (2006). Subsurface Exploration Using the Standard Penetration Test and the Cone Penetrometer Test. *Environmental and Engineering Geoscience*, *7*, 161–179.

Rozitis, B., Maclennan, E., & Emery, J. P. (2014). Cohesive forces prevent the rotational breakup of rubble-pile asteroid (29075) 1950 DA. *Nature*, *512*, 174–176.

Seweryn, K., Skocki, K., Banaszkiewicz, M., Grygorczuk, J., Kolano, M., Kuciski, T., Mazurek, J., Morawski, M., Biaek, A., Rickman, H., & Wawrzaszek, R. (2014). Determining the geotechnical properties of planetary regolith using low velocity penetrometers. *Planetary and Space Science*, *99*, 70 – 83.

Smrekar, S., Catling, D., Lorenz, R., Magalhães, J., Moersch, J., Morgan, P., Murray, B., Presley-Holloway, M., Yen, A., Zent, A., & Blaney, D. (1999). Deep Space 2: The Mars Microprobe Mission. *Journal of Geophysical Research*, *104*, 27013–27030.

Spohn, T., Seiferlin, K., Hagermann, A., Knollenberg, J., Ball, A. J., Banaszkiewicz, M., Benkhoff, J., Gadomski, S., Gregorczyk, W., Grygorczuk, J., Hlond, M., Kargl, G., Kührt, E., Kömle, N., Krasowski, J., Marczewski, W., & Zarnecki, J. C. (2007). Mupus A Thermal and Mechanical Properties Probe for the Rosetta Lander Philae. *Space Science Reviews*, *128*, 339–362.

Surkov, Y. A., & Kremnev, R. S. (1998). Mars-96 mission: Mars exploration with the use of penetrators. *Planetary and Space Science*, *46*, 1689–1696.

Zarnecki, J. C., Leese, M. R., Hathi, B., Ball, A. J., Hagermann, A., Towner, M. C., Lorenz, R. D., McDonnell, J. A. M., Green, S. F., Patel, M. R., Ringrose, T. J., Rosenberg, P. D., Atkinson, K. R., Paton, M. D., Banaszkiewicz, M., Clark, B. C., Ferri, F., Fulchignoni, M., Ghafoor, N. A. L., Kargl, G., Svedhem, H., Delderfield, J., Grande, M., Parker, D. J., Challenor, P. G., & Geake, J. E. (2005). A soft solid surface on Titan as revealed by the Huygens Surface Science Package. *Nature*, *438*, 792–795.